JOURNAL OF APPLIED PHYSICS **113**, 133501 (2013)

# Thermal-wave fields in solid wedges using the Green function method: Theory and experiment

Rui Tai,[1] Jie Zhang,[1] Chinhua Wang,[1,a)] and Andreas Mandelis[2]
[1]*Institute of Modern Optical Technologies, Key Lab of Advanced Optical Manufacturing Technologies of Jiangsu Province and Key Lab of Modern Optical Technologies of Education Ministry of China, Soochow University, Suzhou, Jiangsu 215006, People's Republic of China*
[2]*Center for Advanced Diffusion-Wave Technologies (CADIFT), Department of Mechanical and Industrial Engineering, University of Toronto, M5S 3G8 Ontario, Canada*

(Received 7 February 2013; accepted 14 March 2013; published online 1 April 2013)

In this work, we establish a theoretical model for a cylindrical rod of radius $R$ with opening angle $\theta$ illuminated by a modulated incident beam. The model uses the Green function method in cylindrical coordinates. An analytical expression for the Green function and thermal-wave field in such a solid is presented. The theory is validated in the limit of reducing the arbitrary wedge geometrical structure to simpler geometries. For acute angle wedges, it is shown that the thermal-wave field near the edge exhibits confinement behavior and increased amplitude compared to a flat (reference) solid with $\theta = \pi$. For obtuse angle wedges, it is shown that the opposite is true and relaxation of confinement occurs leading to lower amplitude thermal-wave fields. The theory provides a basis for quantitative thermophysical characterization of wedge-shaped objects and it is tested using an AISI 304 steel wedge and photothermal radiometry detection. © *2013 American Institute of Physics*. [http://dx.doi.org/10.1063/1.4798575]

## I. INTRODUCTION

Laser photothermal radiometry (PTR) has become a powerful tool for the thermophysical characterization and non-destructive evaluation (NDE) of broad classes of materials due to its noninvasive and highly sensitive nature. When compared with other photothermal methods, such as mirage-effect, thermal lens, and/or photothermal beam deflection, PTR is relatively simple in terms of experimental apparatus and is versatile in terms of the sample geometry (e.g., thin/thick or flat/curvature) and physical properties (e.g., transparent/opaque). Thermal waves are generated in a material as a consequence of the absorption of an intensity modulated beam. These highly damped thermal waves propagate through the material and are interrupted or scattered by buried heterogeneities. With increasing PTR applications to the characterization of materials with curved surfaces, studies on curvilinear solids (e.g., cylindrical or spherical samples[1–8]) have been performed in recent years. In this work, we establish a theoretical model by means of the Green function method in cylindrical coordinates for a class of wedge-shaped structures surrounded by walls of radius $R$ illuminated by a modulated incident uniform or Gaussian beam. Thermal waves are generated along the plane wall at distance $r$ $(0 < r < R)$ from the edge, Fig. 1. Based on the theoretical model, the thermal-wave fields of arbitrary-angled wedges and their behavior with respect to modulation frequency at any point on the wall surfaces of the wedge can be obtained. It is found that the thermal-wave field near the edge exhibits different behavior from that at a far distance from the edge. If the position vector $\boldsymbol{r}$ of the measurement point extends far enough away from the edge compared to the thermal diffusion length, the thermal-wave field at this point is reduced to that of a semi-infinite flat sample,[9] as expected.

## II. THEORY

The geometry and coordinates of the wedge-shaped structure are shown in Fig. 1. The Green function for the cylindrical sector of infinite height, radius $R$, and opening angle $\theta$, can be obtained by assuming a spatially impulsive thermal-wave source located at $(r_0, z_0, \phi_0)$ and homogeneous Neumann conditions along all bounding surfaces.

In cylindrical coordinates, the Green function satisfies

$$\frac{1}{r}\frac{\partial}{\partial r}\left[r\frac{\partial}{\partial r}G(r|r_0;\omega)\right]+\frac{\partial^2}{\partial z^2}G(r|r_0;\omega)+\frac{1}{r^2}\frac{\partial^2}{\partial \phi^2}G(r|r_0;\omega)$$
$$-\sigma^2 G(r|r_0;\omega)=-\frac{1}{\alpha r}\delta(r-r_0)\delta(z-z_0)\delta(\phi-\phi_0), \tag{1}$$

where $\omega$ is the angular frequency, $\alpha$ denotes the thermal diffusivity, and $\sigma$ has the physical meaning of the thermal wave number which is defined as $\sigma = \sqrt{i\omega/\alpha}$.

This equation can be solved using separation of variables with $G(r,z,\phi|\vec{r}_0;\omega) = R(r)Z(z)\Phi(\phi)$ and adiabatic (zero thermal-wave flux) boundary conditions on the open flat surfaces forming the corner at $\phi = 0,\ \theta$. This type of boundary condition is justified, in practice, due to the large difference in thermal effusivity between metallic solids and

a)Author to whom correspondence should be addressed. Electronic mail: chinhua.wang@suda.edu.cn.

 

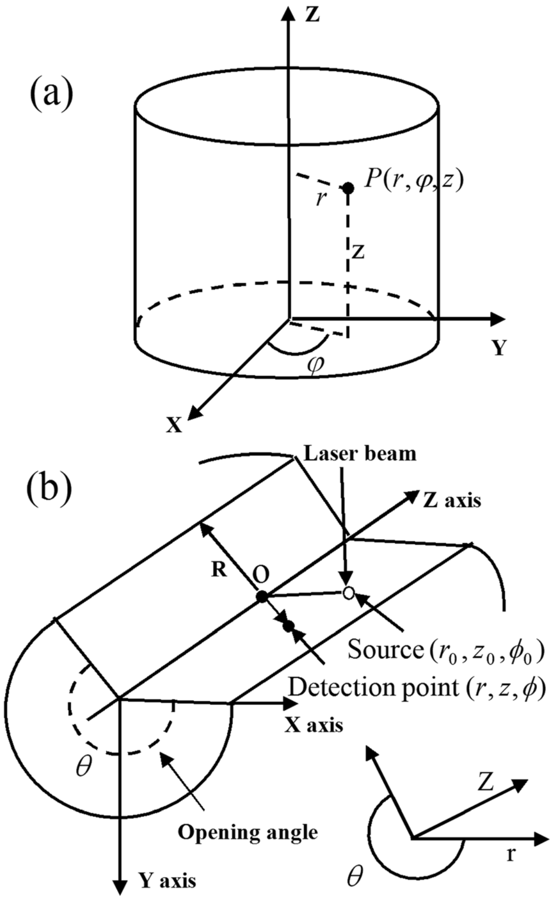


FIG. 1. (a) The relation of an ordinary Cartesian coordinate and a cylindrical coordinate. (b) The geometry and coordinates of a wedge-like solid used in our simulation and experiment.

the surrounding air which is acting as an effectively insulating interface. The resulting ordinary differential equation for the axial component $Z(z)$ is

$$\frac{d^2Z(z)}{dz^2} - (\sigma^2 + \lambda^2)Z(z) = 0, \tag{2}$$

where $\lambda$ is the first separation variable. The bounded solution of Eq. (2) is

$$Z_n(z) = \begin{cases} A_n e^{-\sqrt{\sigma^2+\lambda^2}\cdot(z_0-z)}, & z \le z_0 \\ B_n e^{-\sqrt{\sigma^2+\lambda^2}\cdot(z-z_0)}, & z \ge z_0 \end{cases}; n = 0, 1, 2, \ldots \tag{3}$$

Then by introducing the second separation variable $\mu$, the azimuthal angle equation can be written as

$$\frac{d^2\Phi(\phi)}{d\phi^2} + \mu^2\Phi(\phi) = 0. \tag{4}$$

Applying the homogeneous boundary conditions $\frac{d\Phi}{d\phi}|_{\phi=0} = \frac{d\Phi}{d\phi}|_{\phi=\theta} = 0$ yields the following solutions (eigenfunctions):

$$\Phi_n(\phi) = C_n \cos\left(\frac{n\pi\phi}{\theta}\right); \quad n = 0, 1, 2\ldots \tag{5a}$$

and the associated eigenvalues

$$\mu_n = \frac{n\pi}{\theta}, \quad n = 0, 1, 2, \ldots \tag{5b}$$

Finally, the radial equation is

$$r\frac{d}{dr}\left[r\frac{dR(r)}{dr}\right] + (r^2\lambda^2 - \mu^2)R(r) = 0 \tag{6}$$

with solution bounded at the origin

$$R_n(r) = D_n J_{n\pi/\theta}(\lambda r); \quad n = 0, 1, 2, \ldots, \tag{7}$$

where $J(.)$ represents the Bessel function of the first kind of non-integer order. Equation (7) is subject to a Neumann boundary condition at $r = R$

$$dR_n(r)/dr|_{r=R} = 0. \tag{8}$$

Substituting Eq. (7) in the well-known recursion expression for the derivative of Bessel functions gives

$$(\lambda R)J_{(n\pi/\theta)-1}(\lambda R) = \left(\frac{n\pi}{\theta}\right)J_{(n\pi/\theta)}(\lambda R), \quad n = 0, 1, 2, \ldots \tag{9}$$

For $n = 0$, the eigenvalue equation reduces to

$$J_1(\lambda R) = 0 \Rightarrow \lambda = \beta_m = \gamma_m/R, \quad m = 1, 2, 3, \ldots, \tag{10}$$

where $J_1(\gamma_m) = 0$. For other values of $n$, we require the set of $m$ roots of the Bessel function $J_{n\pi/\theta}(\lambda R)$ which satisfies

$$dJ_{n\pi/\theta}(\lambda r)/dr|_{r=R} = 0. \tag{11}$$

Therefore, $\lambda = \lambda_{nm}$ with $\lambda_{0m} \equiv \beta_{\mathrm{m}}$. This yields the Green function expression

$$G_<(r, z, \phi|\vec{r}_0; \omega) = \sum_{n=0}^{\infty}\sum_{m=1}^{\infty} a_{nm} J_{n\pi/\theta}(\lambda_{nm} r) e^{-\xi_{nm}(z_0-z)} \times \cos\left(\frac{n\pi\phi}{\theta}\right), z \le z_0, \tag{12}$$

$$G_>(r, z, \phi|\vec{r}_0; \omega) = \sum_{n=0}^{\infty}\sum_{m=1}^{\infty} b_{nm} J_{n\pi/\theta}(\lambda_{nm} r) e^{-\xi_{nm}(z-z_0)} \times \cos\left(\frac{n\pi\phi}{\theta}\right), z \ge z_0, \tag{13}$$

where

$$\xi_{nm}(\omega) = \left(\lambda^2{}_{nm} + \frac{i\omega}{\alpha}\right)^{\frac{1}{2}}. \tag{14}$$

Working with these equations and using the orthogonality condition[9]

$$\int_0^R J^2_{n\pi/\theta}(\lambda_{nm} r) r dr = \frac{R^2}{2}\left[1 - \left(\frac{n\pi}{\theta\lambda_{nm} R}\right)^2\right] J^2_{n\pi/\theta}(\lambda_{nm} R), \tag{15}$$

the following Green function is obtained:

$$G(r,z,\varphi|r_0,z_0,\varphi_0;\omega)=\frac{1}{\theta\alpha R^2}\sum_{m=1}^{\infty}\left\{\frac{J_0(\beta_m r)J_0(\beta_m r_0)e^{-\xi_{0m}|z-z_0|}}{\xi_{0m}J_0^2(\beta_m R)}+2\sum_{n=1}^{\infty}\frac{J_{n\pi/\theta}(\lambda_{nm}r)J_{n\pi/\theta}(\lambda_{nm}r_0)e^{-\xi_{nm}|z-z_0|}\cos\left(\frac{n\pi\varphi}{\theta}\right)\cos\left(\frac{n\pi\varphi_0}{\theta}\right)}{\xi_{nm}[1-(n\pi/\theta\lambda_{nm}R)^2]J^2_{n\pi/\theta}(\lambda_{nm}R)}\right\}. \tag{16}$$

For a laser or general optical beam incident at $\phi = 0$, i.e., on the flat surface comprising one of the two walls of the wedge, the thermal-wave field for an opaque material (no volume source) such as a metal wedge is given by

$$T(\vec{r},\omega) = \alpha \oiint_{S_0} [G(\vec{r}|\vec{r}^{\,s}_0;\omega)\vec{\nabla}T(\vec{r}^{\,s}_0,\omega)]\bullet d\vec{S}_0. \tag{17}$$

Assuming that the incident light intensity on the plane surface is uniform, the optical intensity can be expressed as

$$k\vec{n}\bullet\vec{\nabla}T(r,z,0;\omega) = \frac{1}{2}F_0(1+e^{i\omega t}), \tag{18}$$

where $\mathcal{F}_0$ is the optical flux on the surface and $k$ is the thermal conductivity. The thermal-wave field should be single-valued along the axial (length) direction $z$ (at the corner discontinuity $r = 0$), regardless of the location of the source:

$$T(0,z,0;\omega) = T(0,z,\theta;\omega). \tag{19}$$

The final expression for the thermal-wave field is

$$T(r,z,\varphi;\omega) = \frac{F_0}{2\theta kR^2}\sum_{m=1}^{\infty}\left\{\frac{J_0(\beta_m r)}{\xi_{0m}J_0^2(\beta_m R)}\int_{-\infty}^{\infty}e^{-\xi_{0m}|z-z_0|}dz_0\int_0^R J_0(\beta_m r_0)dr_0 + 2\sum_{n=1}^{\infty}\frac{J_{n\pi/\theta}(\lambda_{nm}r)}{\xi_{nm}[1-(n\pi/\theta\lambda_{nm}R)^2]J^2_{n\pi/\theta}(\lambda_{nm}R)}\int_{-\infty}^{\infty}e^{-\xi_{nm}|z-z_0|}dz_0\int_0^R J_{n\pi/\theta}(\lambda_{nm}r_0)dr_0\right\}. \tag{20}$$

If the detection point is $(r,0,0)$ and the opening angle is $\theta = 3\pi/2$, i.e., the two walls of the wedge intersect vertically to form an obtuse right corner, Eq. (20) can be further written as

$$T(r,0,0;\omega) = \frac{F_0}{3\pi kR^2}\sum_{m=1}^{\infty}\left\{\frac{J_0(\beta_m r)}{\xi_{0m}J_0^2(\beta_m R)}\int_{-\infty}^{\infty}e^{-\xi_{0m}|z_0|}dz_0\int_0^R J_0(\beta_m r_0)dr_0 + 2\sum_{n=1}^{\infty}\frac{J_{2n/3}(\lambda_{nm}r)}{\xi_{nm}[1-(2n/3\lambda_{nm}R)^2]J^2_{2n/3}(\lambda_{nm}R)}\int_{-\infty}^{\infty}e^{-\xi_{nm}|z_0|}dz_0\int_0^R J_{2n/3}(\lambda_{nm}r_0)dr_0\right\}. \tag{21}$$

From the structure of this expression, it is seen that the frequency dependence of the thermal-wave field of a wedge illuminated with a uniform light beam is a strong function of the thermophysical parameters of the material as well as the geometrical factors of the solid.

It is computationally very intensive to perform the numerical simulation directly from Eq. (20) because for large values of $n$ and $m$ in $\lambda = \lambda_{nm}$ convergence is very slow. A simplification of Eq. (20) is necessary for numerical computation purposes. For wedge-like solids, the cylindrical boundary curvature can be ignored for $R$ large enough such as $R \to \infty$ is a valid approximation. The following transformation of the first term in Eq. (20) can be made:[9]

$$\frac{1}{R^2}\sum_{n=1}^{\infty}\frac{J_0(\beta_m r)J_0(\beta_m r_0)}{\sqrt{\beta_m{}^2+\sigma^2}J_0{}^2(\beta_m R)} \to \frac{1}{2}\int_0^{\infty}\frac{J_0(\lambda r)J_0(\lambda r_0)}{\sqrt{\lambda^2+\sigma^2}}\lambda d\lambda, \tag{22}$$

where

$$\lim_{R\to\infty}(\beta_m) = \lambda, \tag{23}$$

and the $z$ integration yields

$$\int_{-\infty}^{\infty}e^{-\xi_{0m}|z_0|}dz_0 = \frac{2}{\xi_{0m}}. \tag{24}$$

Using Eqs. (22) and (24), the first term of Eq. (20) can be written in the limit $R \to \infty$ as

$$\frac{1}{R^2}\sum_{n=1}^{\infty}\frac{J_0(\beta_m r)J_0(\beta_m r_0)}{\sqrt{\beta_m{}^2+\sigma^2}J_0{}^2(\beta_m R)}\int_{-\infty}^{\infty}e^{-\xi_{nm}|z_0|}dz_0\int_0^R J_0(\beta_m r_0)dr_0 = \int_0^R dr_0\int_0^{\infty}\frac{J_0(\lambda r)J_0(\lambda r_0)}{\lambda^2+\sigma^2}\lambda d\lambda. \tag{25}$$

The inner integral on the rhs of Eq. (25) has an analytical solution[9]

$$\int_0^{\infty}\frac{J_0(\lambda r)J_0(\lambda r_0)}{\lambda^2+\sigma^2}\lambda d\lambda = \begin{cases} I_0(\sigma r)K_0(\sigma r_0), & 0\le r\le r_0 \\ K_0(\sigma r)I_0(\sigma r_0), & 0\le r_0\le r\end{cases}. \tag{26}$$

Substituting Eq. (26) into Eq. (25), the first term of Eq. (20) can be transformed in the limit $R \to \infty$

$$\frac{1}{R^2}\sum_{n=1}^{\infty}\frac{J_0(\beta_m r)J_0(\beta_m r_0)}{\sqrt{{\beta_m}^2+\sigma^2}\,J_0{}^2(\beta_m R)}\int_{-\infty}^{\infty}e^{-\xi_{0m}|z_0|}dz_0\int_0^R J_0(\beta_m r_0)^{dr_0}=\int_0^r K_0(\sigma r)I_0(\sigma r_0)dr_0+\int_r^R I_0(\sigma r_0)K_0(\sigma r)dr_0. \tag{27}$$

Following the same procedure, the second term of Eq. (20) can also be written in the limit $R\to\infty$ as

$$2\sum_{n=1}^{\infty}\left\{\frac{J_{2n/3}(\lambda_{nm}r)}{\xi_{nm}[1-(2n/3\lambda_{nm}R)^2]J^2_{2n/3}(\lambda_{nm}R)}\int_{-\infty}^{\infty}e^{-\xi_{nm}|z_0|}dz_0\int_0^R J_{2n/3}(\lambda_{nm}r_0)dr_0\right\}\to$$
$$2\sum_{n=1}^{\infty}\left\{\int_0^r K_{n\pi/\theta}(\sigma r)I_{n\pi/\theta}(\sigma r_0)dr_0+\int_r^R I_{n\pi/\theta}(\sigma r)K_{n\pi/\theta}(\sigma r_0)dr_0\right\}. \tag{28}$$

The final operational expression for the thermal-wave field in the limit of infinite radius of curvature is given as

$$T(r,0,0;\omega)=\frac{F_0}{2k\theta}\left\{\begin{array}{l}\displaystyle\int_0^r[I_0(\sigma r_0)K_0(\sigma r)+2\sum_{n=1}^{\infty}I_{n\pi/\theta}(\sigma r_0)K_{n\pi/\theta}(\sigma r)]dr_0\\ \displaystyle+\int_r^{\infty}[I_0(\sigma r)K_0(\sigma r_0)+2\sum_{n=1}^{\infty}I_{n\pi/\theta}(\sigma r)K_{n\pi/\theta}(\sigma r_0)]dr_0\end{array}\right\}. \tag{29}$$

If the exciting optical source is a Gaussian laser beam centered at $(\rho_0,0,0)$, the thermal-wave flux into the solid on the flat surface $\phi=0$ is

$$k\hat{n}\bullet\vec{\nabla}T(r,z,0;\omega)=\frac{1}{2}F_0\exp\{-[(r-\rho_0)^2+z^2]/W^2\}(1+e^{i\omega t}). \tag{30}$$

In this case, the expression for the thermal-wave field becomes

$$T(r,z,\varphi;\omega)=\frac{F_0}{2\theta kR^2}\sum_{m=1}^{\infty}\left\{\frac{J_0(\beta_m r)}{\xi_{0m}J_0^2(\beta_m R)}\int_{-\infty}^{\infty}e^{-\xi_{0m}|z-z_0|-(z_0/W)^2}dz_0\int_0^R J_0(\beta_m r_0)e^{-(r_0-\rho_0)^2/W^2}dr_0\right.$$
$$\left.+2\sum_{n=1}^{\infty}\frac{J_{n\pi/\theta}(\lambda_{nm}r)\cos\left(\frac{n\pi\varphi}{\theta}\right)}{\xi_{nm}[1-(n\pi/\theta\lambda_{nm}R)^2]J^2_{n\pi/\theta}(\lambda_{nm}R)}\int_{-\infty}^{\infty}e^{-\xi_{nm}|z-z_0|-(z_0/W)^2}dz_0\int_0^R J_{n\pi/\theta}(\lambda_{nm}r_0)e^{-(r_0-\rho_0)^2/W^2}dr_0\right\}. \tag{31}$$

If the incident Gaussian beam is further assumed to be a cylindrical Gaussian beam and the medium fully opaque, the light intensity along the $z$ axis is uniform and the $z$ component can be ignored, i.e.,

$$k\hat{n}\bullet\vec{\nabla}T(r,z,0;\omega)=\frac{1}{2}F_0\exp\{-[(r-\rho_0)^2+z^2]/W^2\}(1+e^{i\omega t}). \tag{32}$$

Equation (31) for the temperature field at $z=0$ and $\phi=0$ reduces to

$$T(r,0,0;\omega)=\frac{F_0}{2\theta kR^2}\sum_{m=1}^{\infty}\left\{\frac{J_0(\beta_m r)}{\xi_{0m}J_0^2(\beta_m R)}\int_{-\infty}^{\infty}e^{-\xi_{0m}|z_0|}dz_0\int_0^R J_0(\beta_m r_0)e^{-(r_0-\rho_0)^2/W^2}dr_0\right.$$
$$\left.+2\sum_{n=1}^{\infty}\frac{J_{n\pi/\theta}(\lambda_{nm}r)}{\xi_{nm}[1-(n\pi/\theta\lambda_{nm}R)^2]J^2_{n\pi/\theta}(\lambda_{nm}R)}\int_{-\infty}^{\infty}e^{-\xi_{nm}|z_0|}dz_0\int_0^R J_{n\pi/\theta}(\lambda_{nm}r_0)e^{-(r_0-\rho_0)^2/W^2}dr_0\right\} \tag{33}$$

which can be further transformed in the limit $R\to\infty$

$$T(r,0,0;\omega)=\frac{F_0}{2k\theta}\left\{\int_0^r[I_0(\sigma r_0)K_0(\sigma r)+2\sum_{n=1}^{\infty}I_{n\pi/\theta}(\sigma r_0)K_{n\pi/\theta}(\sigma r)]e^{-(r_0-\rho)^2/W^2}dr_0\right.$$
$$\left.+\int_r^{\infty}[I_0(\sigma r)K_0(\sigma r_0)+2\sum_{n=1}^{\infty}I_{n\pi/\theta}(\sigma r)K_{n\pi/\theta}(\sigma r_0)]e^{-(r_0-\rho)^2/W^2}dr_0\right\}. \tag{34}$$

## III. NUMERICAL CALCULATIONS

To highlight the net effects of the presence of the wedge in simulations and experimentally, the amplitude and phase of the surface thermal-wave field are normalized to the corresponding amplitude and phase of a flat semi-infinite solid of the same material (AISI 304 stainless steel). The incident light is assumed to be a plane wave. The thermophysical parameters of AISI 304 stainless steel are $k = 16.3$ W/mK, $\alpha = 4.1 \times 10^{-6}\,\mathrm{m^2/s}$.[10] Figure 2 shows the thermal-wave fields at various distances ($r$) from the edge on the surface $\phi = 0^\circ$. The opening angle is $\theta = 3\pi/2$. It is observed that the effect of the corner on the thermal-wave field becomes more pronounced as the detection point moves closer to the corner. If the detection point is far enough away from the corner (i.e., $r$ is large compared to the thermal diffusion length), the thermal-wave field at this point reduces to that of a semi-infinite flat solid, i.e., the normalized amplitude and phase are toward 1 and 0, respectively, in Fig. 2, which is as expected. At distances very close to the obtuse right corner (i.e., within one thermal diffusion length), the normalized amplitude decreases because physically the 270° corner acts as a thermal-wave sink in comparison with the flat reference solid: the solid material extends vertically above the horizontal plane to form the wall at $\theta = 3\pi/2$ thereby amounting to additional upward degrees of freedom for diffusive thermal waves, compared to the flat case $\theta = \pi$. As a result, the normalized amplitude for the right angle case for the low frequency range where the thermal diffusion length overlaps the corner coordinate is smaller than that for the $\theta = \pi$ case due to decreased confinement in the half space below the surface plane. There is a hint of thermal-wave interference due to the presence of the right corner (diffraction around the corner) before the two geometries converge to the same thermal-wave amplitude at high frequencies where the thermal diffusion length is short compared to the distance from the corner. Similarly, the normalized phase exhibits a lag for several degrees as the thermal wave extends farther away from the radial location, proportionately shifting away the thermal centroid.

Different wedge angles will result in measurably different thermal-wave distributions especially around the edge region, provided the distance to the edge is commensurate with the thermal diffusion length. Figure 3 shows several thermal-wave fields in structures with different opening angles. The detection point is located at $\phi = 0^\circ$ and $r = 1$ mm. It is seen that when $\theta = \pi/2$, i.e., the structure contains a vertical solid edge (acute right corner), the normalized thermal-wave field, both amplitude and phase, is coincident with that in a semi-infinite flat structure. This is consistent with numerical simulations based on the method of images (Ref. 9, p. 294). This identity between $\theta = \pi/2$ and $\theta = \pi$ geometries shown in Fig. 3 is also consistent with earlier results using the method of images.[11] The apparent paradox of these thermal-wave field coincidences is due to the adiabatic (zero flux) boundary condition along the vertical wall: this condition does not allow for a horizontal thermal-wave flux component across the interface, thereby producing a thermal-wave field at the coordinate point $r = 0$ in the right corner geometry which is identical to the flat

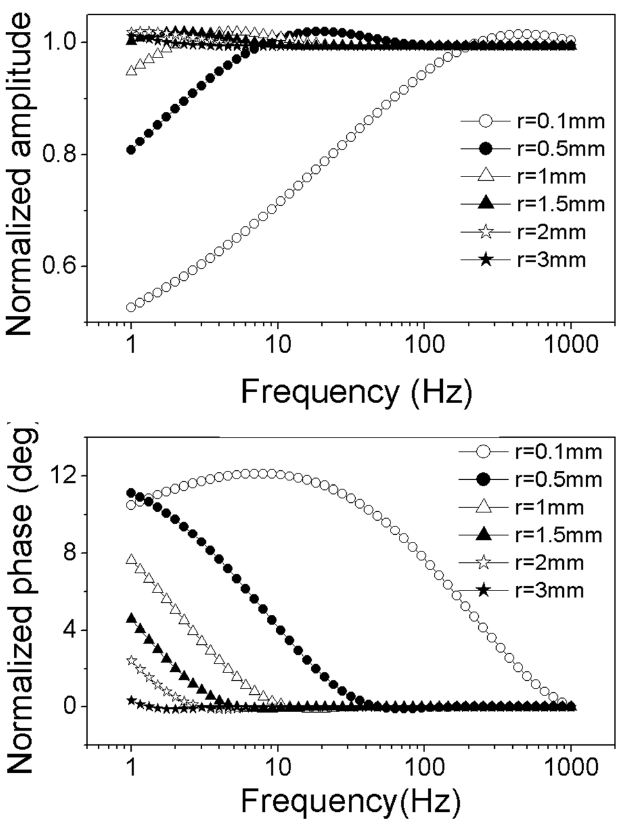


FIG. 2. The normalized thermal-wave fields at different distances ($r$) from a $\theta = 3\pi/2$ wedge.

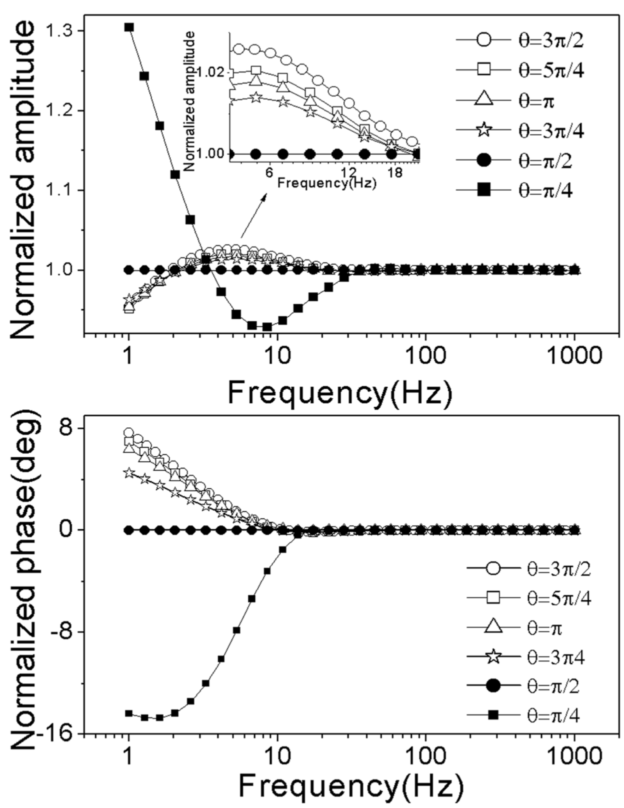


FIG. 3. The normalized thermal-wave fields of a wedge structure with different opening angles $\phi$.

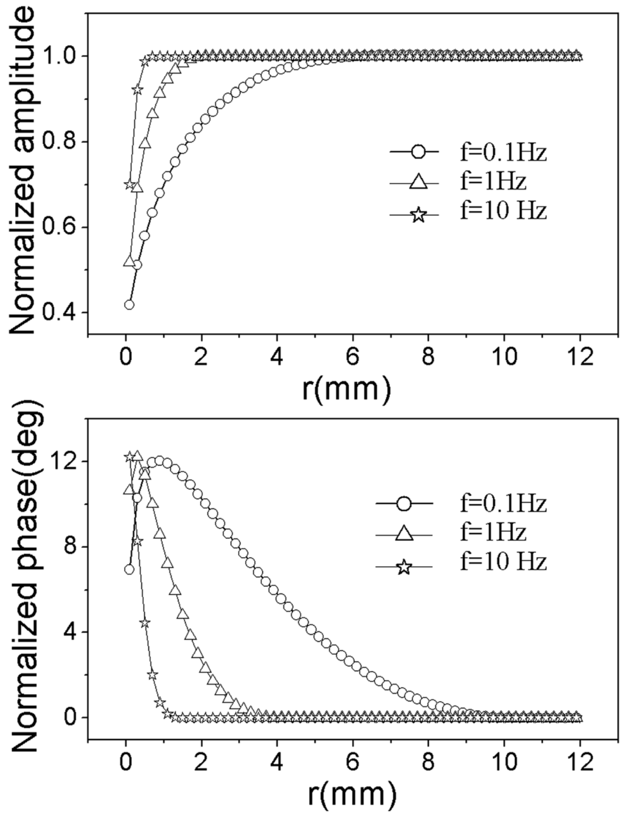


FIG. 4. The scanned and normalized thermal-wave field along the radial direction at different frequencies.

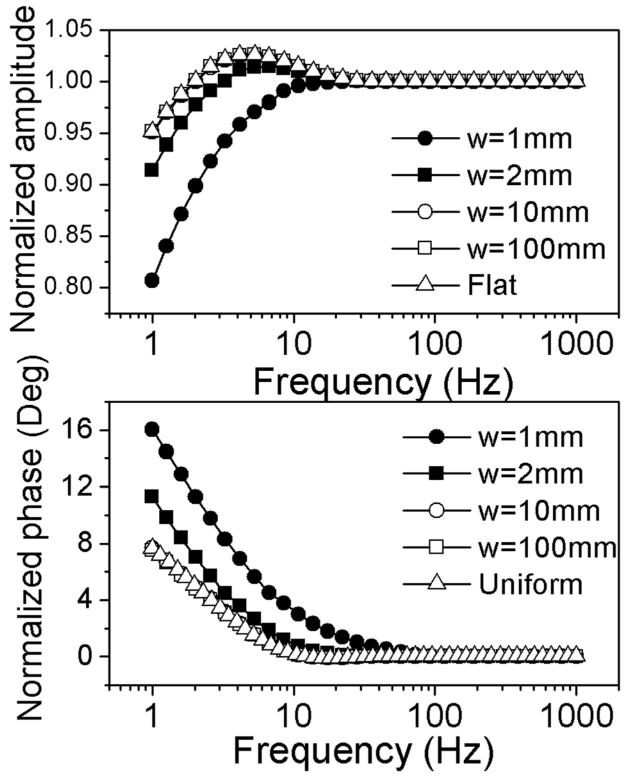


FIG. 5. Frequency dependence of the thermal-wave field from a sample with an obtuse right corner ($\theta = 3\pi/2$) at $r = 1$ mm, illuminated with Gaussian laser beams of various spotsizes. The curves are normalized with a semi-infinite flat sample of the same material illuminated with a uniform beam.

solid which also does not sustain a horizontal flux component. This situation has been discussed in detail in Ref. 9, pp. 274–276.

Figure 4 shows the behavior of the normalized thermal-wave field near the obtuse right corner $\theta = 3\pi/2$ when the detection point is scanned along the radial direction at various frequencies. The results can provide a theoretical signal reference near the corner for noncontact and nondestructive detection. The discussion accompanying Fig. 2 is also valid here. It is observed that at high frequencies and/or longer distances away from the corner, such that the decreased thermal diffusion length is shorter than the distance to the corner, the relaxation of the thermal-wave confinement provided by the flat surface solid makes little difference in the amplitude and phase of the field in the solid with $\theta = 3\pi/2$.

Finally, we present the thermal-wave field of a surface illuminated by a cylindrical Gaussian laser beam. In the simulation, the spotsize W is assumed to be 1 mm, 2 mm, 10 mm, 100 mm (i.e., close to infinite), respectively. The beam center is fixed at $\rho = 1$ mm, which is also the detection point in the simulation. The simulation results are shown in Fig. 5. It is seen that as the spotsize increases, both amplitude and phase move toward the response of the obtuse right corner illuminated with a homogeneous beam. When the laser spotsize W is 100 mm, the two lines overlap, as expected, because the beam spatial profile distribution converges to a uniform distribution. The Green-function sensitivity to beam spotsize demonstrates the necessity to carefully characterize the incident beam profile and size for accurate quantitative photothermal thermophysical studies.

## IV. EXPERIMENTAL AND RESULTS

To verify the foregoing theoretical model, PTR experiments were performed using a wedge with an obtuse right corner ($\theta = 3\pi/2$), made of AISI 304 steel with composition C 0.07%, Si 1.0%, Mn 2.0%, Cr 17.0%–19.0%, Ni 8.0%–11.0%, S 0.03%, P 0.035%. The experimental system is shown in Fig. 6. The thermal-wave source was a high-power semiconductor laser (~30 W). The output of the laser was modulated by a periodic current, the frequency of which was controlled by a computer generated waveform which

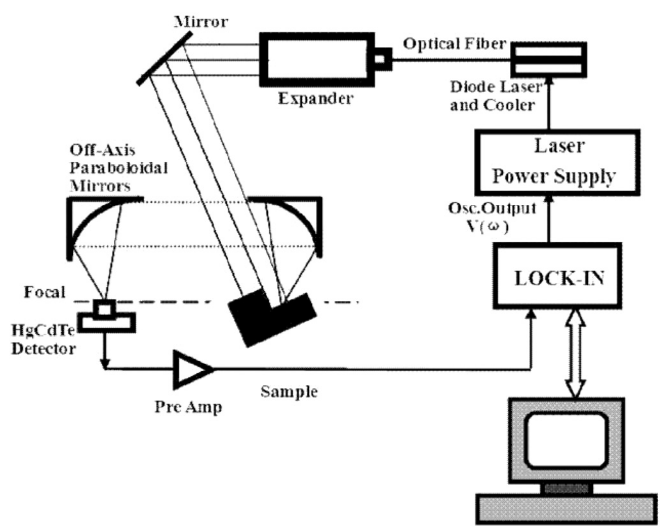


FIG. 6. The experimental PTR setup.

also served as the lock-in reference signal. The beam was expanded, collimated, and then focused onto the surface of the sample. Because the size of the beam (diameter = 30 mm) was much larger than the thermal diffusion length (∼2.8 mm at 1 Hz), the beam can be considered uniform. The harmonically modulated infrared radiation from the sample surface was collected by an off-axis paraboloidal mirror system and detected by a HgCdTe detector. The signal from the detector was amplified with a low-noise preamplifier and then fed into a lock-in amplifier which was interfaced with the personal computer.

In the experiments, the sample was positioned carefully at the focal point of the paraboloidal mirror. The laser beam was perpendicular to the surface ($\phi = 0$) of the sample. The starting point was set as $\Delta$ (the distance between the corner ($r = 0$) and the detection point). The detection point was scanned along the radial direction. Adjusting the distance of the detection point ($r = \Delta + r'$, where $r'$ is the well controlled adjustable distance relative to position $\Delta$ of the first point), the thermal-wave field signal was obtained at various positions. The absolute position parameter $\Delta$ and the thermal diffusivity of the sample were measured from those signals as the result of best-fitting to the theory as described below. From the experimental results, it was obvious that the effect of the corner on the thermal-wave field followed the expected behavior shown in Figs. 2 and 5 as the detection point moved closer to the corner. The signal was normalized to that from a semi-infinite flat sample of the same material.

Four sets of experimental data were measured at positions $r = \Delta$, $r = \Delta + 0.1$ mm, $r = \Delta + 0.3$ mm, and $r = \Delta + 1.3$ mm, respectively. The data were fitted to the theoretical model, Eq. (29). The fitting parameters were $\Delta$ and $\alpha$. The experimental data and the fitted results are shown in Fig. 7, while the detailed best-fitted parameters are shown in Table I. Figure 7 shows that the noise of the normalized experimental data is relatively large especially at low frequencies. The relatively low signal-to-noise ratio in the normalized amplitude and phase is mainly due to the noise addition and the large background subtraction incurred in the normalization process. Nevertheless, Fig. 7 shows good agreement between the theoretical and experimental results.

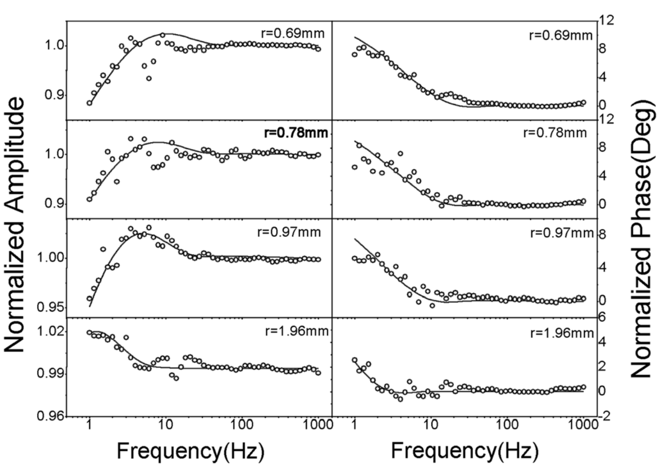


FIG. 7. PTR results. Symbols: experimental data; solid lines: theoretical fits.

TABLE I. Best-fit results of the obtuse right-corner sample based on the theoretical model Eq. (29). Averaging the four thermal diffusivity yields $\alpha_{Avg} = 3.93 \pm 0.4 \times 10^{-6}$ m²/s.

| $r'$ (mm) | $\Delta$ (mm) | $\alpha$ (m²/s) |
|---|---|---|
| 0.0 | 0.694 | $3.90 \times 10^{-6}$ |
| 0.1 | 0.704 | $3.51 \times 10^{-6}$ |
| 0.3 | 0.673 | $4.02 \times 10^{-6}$ |
| 1.3 | 0.693 | $4.29 \times 10^{-6}$ |

The main physical effects are: (1) overall decrease in thermal-wave amplitude and concomitant increase in phase lag very near the obtuse 270° corner (thermal diffusion length longer than $\Delta$) due to the additional diffusion-wave degrees of freedom available beyond the corner, and (2) the slight diffractive interferometric amplitude increase preceding the drop, at frequencies corresponding to thermal diffusion lengths on the order of $\Delta$. As expected, the larger the distance $r$, the lower the frequency range within which these interfacial effects occur because longer thermal diffusion lengths, $\mu(f)$, are required to satisfy the same relationship ($\mu(f) \geq \Delta$) to the changing value of $\Delta$.

Table I shows the best-fitted thermal diffusivity values and position parameters $\Delta$ at various locations with respect to the corner. The result of the thermal diffusivity value is $(3.93 \pm 0.38) \times 10^{-6}$ m²/s, averaged over the four best-fitted values at each distance from the corner. This value is in good agreement with $4.10 \times 10^{-6}$ m²/s reported in the literature.[10]

## V. CONCLUSIONS

In summary, we have developed an analytical theory for the thermal-wave field of wedge-shaped solid structure with arbitrary opening angle using the Green function method subject to boundary conditions of the second kind at the open surfaces. The Green function is derived and a general expression for the thermal-wave field of wedge-shaped solids irradiated with an incident optical source of arbitrary radial intensity distribution was obtained. The photothermal field model of a finite-radius cylindrical solid wedge was further extended to a solid of infinite radius of curvature, a simplification of the theory for computational purposes. Relative thermal-wave amplitudes and phases were obtained using acute and obtuse-angle wedge responses "normalized" to that of a flat solid of the same material. This work offers a solid theoretical basis for characterizing wedge-shaped solids of relevance to industrial manufacturing.

## ACKNOWLEDGMENTS

This work was supported by a grant from the National Natural Science Foundation of China Contract No. 60877063, Scientific Research Foundation for Returned Scholars, Ministry of Education of China, and the project of the Priority Academic Program Development (PAPD) of Jiangsu Higher Education Institutions. The Canada Research Chairs and the Natural Sciences and Engineering Research Council of Canada are gratefully acknowledged for their support through a CRC Tier I award and a Discovery Grant, respectively, to A.M.

[1]C. Wang, A. Mandelis, and Y. Liu, J. Appl. Phys. **96**, 3756 (2004).
[2]C. Wang and A. Mandelis, Rev. Sci. Instrum. **78**, 054902 (2007).
[3]C. Wang, Y. Liu, A. Mandelis, and J. Shen, J. Appl. Phys. **101**, 083503 (2007).
[4]G. Xie, Z. Chen, C. Wang, and A. Mandelis, Rev. Sci. Instrum. **80**, 034903 (2009).
[5]G. Xie, J. Zhang, L. Liu, C. Wang, and A. Mandelis, J. Appl. Phys. **109**, 113534 (2011).
[6]A. Salazar, F. Garrido, and R. Celorrio, J. Appl. Phys. **99**, 066116 (2006).
[7]A. Salazar and R. Celorrio, J. Appl. Phys. **100**, 113535 (2006).
[8]N. Madariaga and A. Salazar, J. Appl. Phys. **101**, 103534 (2007).
[9]A. Mandelis, *Diffusion-Wave Fields: Mathematical Methods and Green Function* (New York, Springer, 2001), p. 90.
[10]J. N. Sweet, E. P. Roth, and M. Moss, Int. J. Thermophys. **8**(5), 593–606 (1987).
[11]L. C. Aamodt and J. C. Murphy, Appl. Opt. **21**, 111 (1982).